Geophysical Journal International

Geophys. J. Int. (2022) **231,** 15–26
Advance Access publication 2022 May 06
GJI Geomagnetism, Rock Magnetism and Palaeomagnetism

https://doi.org/10.1093/gji/ggac172

A new power spectrum and stochastic representation for the geomagnetic axial dipole

Mayuri Sadhasivan[1,2] and Catherine Constable[1]

[1]*Institute of Geophysics & Planetary Physics, Scripps Institution of Oceanography, University of California, San Diego, La Jolla, CA* 92093-0225, *USA. E-mail: masadhasivan@ucsd.edu*

[2]*Morton K. Blaustein Department of Earth and Planetary Sciences, Zanvyl Krieger School of Arts and Sciences, Johns Hopkins University, Baltimore, MD* 21218, *USA*

Accepted 2022 May 3. Received 2022 April 22; in original form 2022 February 3

SUMMARY

Earth's internal magnetic field is dominated by the contribution of the axial dipole whose temporal variations are wide ranging and reflect characteristic timescales associated with geomagnetic reversals and large scale palaeosecular variation, ranging down to decadal and subannual field changes inferred from direct observations. We present a new empirical power spectrum for the axial dipole moment based on composite magnetic records of temporal variations in the axial dipole field that span the frequency range 0.1 to 5×10^5 Myr^{-1} (periods from 10 million to 2 yr). The new spectrum is used to build a stochastic representation for these time variations, based on an order 3 autoregressive (AR) process and placed in the context of earlier stochastic modelling studies. The AR parameter estimates depend on the frequency of transitions in the spectral regime and may be influenced by Ohmic diffusion, advection and torsional oscillations in Earth's core. In several frequency ranges across the interval 200–5000 Myr^{-1} (5000 to 200 yr periods) the empirical power spectrum lies above the AR3 model and may be influenced by Magneto–Coriolis (MC) waves in Earth's core. The spectral shape and parameter estimates provide a potentially useful guide for developing assessments of whether numerical dynamo simulations meet criteria for being considered Earth like.

Key words: Magnetic field variations through time; Palaeointensity; Palaeomagnetic secular variation; Statistical methods; Time-series analysis.

1 INTRODUCTION

Earth's time-varying internal magnetic field, known as the geodynamo, is sustained by vigorous convection in Earth's electrically conducting, liquid-iron outer core (Backus *et al.* 1996). Fluid motions in the outer core are driven by thermal and chemical buoyancy lifting and twisting the fluid and creating electric currents that can reinforce and regenerate the field. These flows drive continual temporal variations in field strength over timescales ranging from days to hundreds of millions, perhaps even billions, of years. Measurement of the field strength over such a wide range relies on multiple different approaches. Satellite, observatory and survey measurements provide direct observations of field strength and direction since the mid 19th century (Finlay *et al.* 2016; Alken *et al.* 2021). Magnetic data from observatories, surveys and ship records extending back to the 16th century allow access to centennial variations (Jackson *et al.* 2000). Earlier changes must be recovered from archeomagnetic, volcanic and sedimentary palaeomagnetic records which are used to study millennial scale (Constable *et al.* 2016; Panovska *et al.* 2018; Senftleben 2020) to million year variations (Ziegler *et al.* 2011). At longer timescales magnetic anomalies recorded in the seafloor crust provide a record of the timing of geomagnetic polarity reversals (Cande & Kent 1995; Ogg 2012).

The geomagnetic field at Earth's surface is traditionally represented via a spherical harmonic expansion in terms of time varying Gauss coefficients, $\{g_l^m(t), h_l^m(t)\}$ of degree l and order m. Numerous previous studies have made estimates for these Gauss coefficients from field observations and shown that in the resulting geomagnetic field models, the coefficient $g_1^0(t)$ has the largest time-averaged magnitude and, given the field's propensity to reverse polarity on geological timescales, it also has the greatest dynamic range over time among the various $\{g_l^m(t), h_l^m(t)\}$ describing the observed field (Jackson *et al.* 2000; Ziegler *et al.* 2011; Olsen *et al.* 2014; Constable *et al.* 2016; Panovska *et al.* 2018).

In this work we focus our attention on variations in the magnitude of the dominant axial dipole, $g_1^0(t)$, as illustrated in Fig. 1, and further discussed in Section 2. An equivalent representation in terms of the axial dipole moment (ADM), represented in this paper by

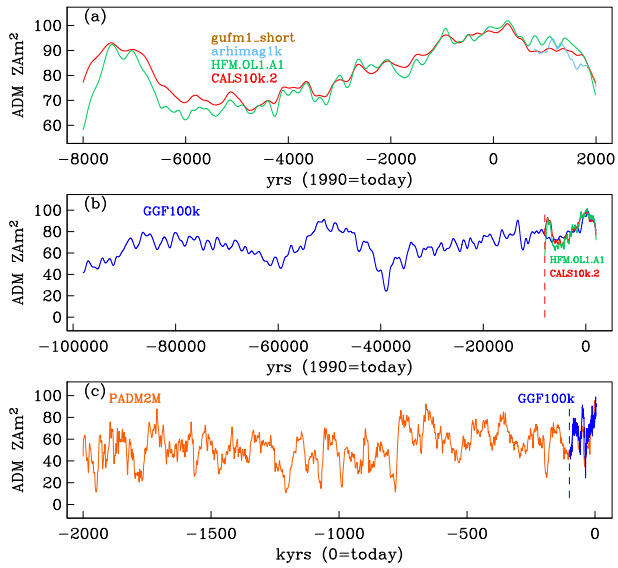

Figure 1. Time-series for axial dipole variations drawn from models *gufm1*, *arhimag1k*, *HFM.OL1.A1*, *CALS10k.2*, *GGF100k* and *PADM2M*. See text for details. Vertical dashed lines in (c) and (b) indicate where oldest part of (b) and (a), respectively, would take over on the timeline.

$p(t)$, is often used as a scalar proxy for the overall strength of the geomagnetic field:

$$p(t) = \frac{4\pi r_e^3}{\mu_0}|g_1^0(t)|, \tag{1}$$

where r_e is Earth's radius and μ_0 is the magnetic permeability in a vacuum. The power spectrum of the ADM has been previously used to evaluate the frequency content of large scale variations in geomagnetic field strength based on observations (see e.g. Constable & Johnson 2005). Such studies enable treating $p(t)$ as a stochastic process suitable for statistical analyses and comparisons with output from numerical dynamo simulations (see e.g. Olson *et al.* 2012; Davies & Constable 2014; Avery *et al.* 2019). We revisit the utility of stochastic modelling in this paper.

1.1 Why stochastic modelling is a useful approach

The spherical harmonic description of Earth's field is derived from the pre-Maxwell's equation and might seem to imply that a deterministic representation of the geomagnetic field as a function of space and time lies within our grasp so that we should be able to link various physical processes in Earth's outer core to changes in the ADM with time. This is not yet the case, especially for the long timescales that we are interested in here.

Normally we might seek out periodic or quasi-periodic cycles in geomagnetic field data as is often done for other geophysical data—for example, the solar magnetic field and Earth's atmosphere exhibit detectable, quasi-periodic variability (Bengtsson 2003; Di Lorenzo *et al.* 2010; Hathaway 2015). But once a timescale for geomagnetic reversals was established (Cox *et al.* 1964), it became apparent that reversals do not occur on a regular or predictable basis. So Cox (1968) initially proposed that the magnetostratigraphic sequence of geomagnetic reversals might be described as a memoryless Poisson process. In such a process, the probability that a new reversal will occur is totally independent of the record of previous reversals. The time interval between adjacent reversals is described by an exponential probability distribution function where the e-folding parameter provides a measure of reversal rate.

Later refinements to the Poisson model acknowledged that the reversal rate actually changed through time (McFadden *et al.* 1988; Constable *et al.* 1998; Constable 2000); thus the e-folding parameter is time-dependent. Furthermore, it is clear that the occurrences of geomagnetic reversals cannot be considered memoryless as is considered appropriate, for example, in the classic Poisson application of describing radioactive decay processes. Hence, a memoryless Poisson process is too simple to describe the geomagnetic reversal record. The initial Poisson description nevertheless set the stage for representing geomagnetic field variability as a stochastic process, that is where at least part of the variations are random (or at least unpredictable) with respect to time.

Geomagnetic field variations on timescales shorter than the millions of years represented in the reversal timescale also appear to lack predictability. For example, palaeomagnetic sedimentary records exhibit large, irregular variations in regional and dipolar field strength over 10–100 kyr timescales. And despite numerous attempts to identify periodic processes in field records and correlate them with external forcing processes such as Milankovitch climate variations (Yamazaki & Oda 2002), tektite bombardments (Glass & Heezen 1967) or claims of identifying millennial periodicity (Nilsson *et al.* 2011, 2020) no strong periodic signal is found in the ADM (Constable & Johnson 2005). Recent efforts seeking to predict reversals from precursory geomagnetic dipole moment variations (Gwirtz *et al.* 2021) have met with limited success.

The source of the unpredictable temporal variability in the geomagnetic field is the geodynamo, driven by complex processes in the outer core that are described by the magnetic induction equation,

$$\frac{\mathrm{d}\mathbf{B}}{\mathrm{dt}} = \nabla \times (\mathbf{v} \times \mathbf{B}) + \frac{1}{\mu_o \sigma}\nabla^2 \mathbf{B}, \tag{2}$$

where $\mathbf{B}$ is the magnetic field, $\mathbf{v}$ is the core fluid velocity, σ is the electrical conductivity of the outer core fluid and $\mu_o = 4\pi \times 10^{-7}$ H m^{-1} is the magnetic permeability in a vacuum. The magnetic induction equation shows that temporal variations in the geomagnetic field arise from an imbalance between advection of the field by fluid flow in Earth's outer core (the cross-product term) and Ohmic diffusion (the Laplacian term, Backus *et al.* 1996).

Variations due to dominance of either advection or Ohmic diffusion can occur on quite different timescales. Additionally, non-linear coupling between the magnetic field and outer-core flow field in the Navier–Stokes and temperature equations (Moffatt 1978) set the stage for turbulent chaotic small-scale processes that cannot be easily predicted even in numerical dynamo simulations. Thus, we turn to continuous stochastic models of the geomagnetic field, expanding upon ideas that have evolved from the simple Poisson model discussed above.

Continuous stochastic models were originally developed to describe a water molecule that moves under the combined influence of viscous fluid resistance and random collisions with other water molecules. The viscous force is treated as a deterministic process (i.e. with a known mathematical description) while the collisions are treated as a random-noise process (Langevin 1908). For our purposes, the magnetic induction equation acts as a deterministic process while fluid turbulence in Earth's outer core causes random fluctuations in the geomagnetic field. Hence, the interplay between advection, Ohmic diffusion and fluid turbulence provides a plausible physical basis for stochastic descriptions of the time-varying geomagnetic field.

The Langevin and Fokker–Planck equations can both describe an ADM $p(t)$ that has a deterministic, equilibrium behaviour and random fluctuations away from the equilibrium. Previous researchers used the Langevin (Buffett *et al.* 2013; Buffett & Matsui 2015) and Fokker–Planck (Schmitt *et al.* 2001; Hoyng *et al.* 2002) equations to model the frequency spectrum and the temporally varying probability distribution of the ADM, respectively. These authors compared their results with the spectra and distributions derived from various time-series including some of those in Fig. 1.

Later adjustments made to these models accounted for the loss of temporal resolution in palaeomagnetic observations caused by record stacking and gradual acquisition of sedimentary magnetization (Buffett & Puranam 2017). Most recently, Morzfeld & Buffett (2019) implemented a feature-based maximum likelihood approach to estimate the Langevin model parameters and compared their results with various published palaeomagnetic time-series: PADM2M, SINT2000 and CALS10k.2 (Valet *et al.* 2005; Ziegler *et al.* 2011; Constable *et al.* 2016).

Several other studies compared the results of stochastic models with numerical (Buffett *et al.* 2014; Buffett & Matsui 2015) and experimental (Berhanu *et al.* 2007; Pétrélis & Fauve 2008; Pétrélis & Fauve 2010) dynamos. These comparisons among the statistical properties of geomagnetic field data, of experimental dynamos and of numerical dynamo simulations, provide a potential pathway to evaluate which simulations and experiments have Earth-like properties. Finally, some studies have used stochastic models to describe non-dipole field variations (Bouligand *et al.* 2016).

In this work we further develop stochastic geomagnetic models for the dipole to cover a broad range of frequencies and physical processes in Earth's core. In Section 2, we present recent time-series for the ADM that have been derived from observations and we provide a new composite power spectrum for the ADM that extends from timescales of years to millions of years. In Section 3, we extend previously published stochastic models to this broader frequency range. Section 4 provides a comparison of our model with the composite spectrum to estimate values for our model parameters. In Section 5, we discuss physical connections between our model parameters and the geodynamo. Finally, in Section 6 we present our conclusions and propose future work extending from this study.

2 PALAEOMAGNETIC RESULTS

2.1 Time-series

Over the past two decades there have been significant improvements in both palaeomagnetic data compilations and palaeofield modelling that provide us with time-series for the magnitude of g_1^0 on a range of different timescales. The corresponding ADM variations, $p(t)$, from five time-varying field models as in eq. (1), are plotted in Figs 1(a) and (b). *GGF100K* (Panovska *et al.* 2018) covers the interval 0-100 ka, and *HFM.OL1.A1* and *CALS10k.2* (Constable *et al.* 2016) spanning 0–10 kyr are based on palaeomagnetic data. *arhimag1k* covering the millenium from 1000 to 2000 CE is built from a combination of direct observations and archeomagnetic and volcanic data (Senftleben 2020). *gufm1.short* spans the observational period that includes direct intensity measurements in addition to directional observations of the field (1840–1990 CE). In Fig. 1(c), *PADM2M* (Ziegler *et al.* 2011) is a reconstruction of $p(t)$ based on both absolute and relative palaeointensity data covering the past 2 Myr.

Each of the time-series in Fig. 1 has a cubic spline parametrization in time (see for example, Korte & Constable 2003) and has been developed from regularized inversion of globally distributed data covering the respective timelines. Their respective temporal resolutions depend on the data quality and available chronological constraints, and the spline knot spacing, ranging from 2.5 to 1000 yr, has been chosen accordingly. The details are provided in Table 1, where column 1 gives the name of the time-series, followed by the total time spanned by the time-series in column 2, and column 3 provides the equal knot spacing for the cubic spline representation of temporal variations, and thus a clear limitation on the temporal resolution. The sampling interval given in column 4 is used for the model predictions after spline interpolation that are plotted in Fig. 1 and is what we used in our initial estimates of the power spectrum (see Section 2.2. This sampling interval is much shorter than the expected model resolution (column 5), which is our estimate of the shortest plausible timescale on which we could interpret the spectral structure. This is typically controlled by factors such as sedimentation rate, and ability to identify coeval times across different geographic regions. This is discussed further in Section 2.2, together with column 6 and 7 in Table 1.

It should be noted that there are some discrepancies in the models especially in regions where models with shorter time spans overlap the longer models with poorer temporal resolution: for example *arhimag1k* has more detail than either *CALS10k.2* or *HFM.OL1.A1*; the high values after 10 ka in *CALS10k.2* are muted and come earlier in *GGF100k*; and *CALS10k.2* has lower temporal variability than *HFM.OL1.A1* throughout the record (Constable *et al.* 2016).

In contrast to the time-series in Fig. 1 the magnetostratigraphic timescale of Ogg (2012) seen in Fig. S1 only provides polarity information in the form of timing of geomagnetic reversals. In our modelling we follow the strategy used by Constable & Johnson (2005) and suppose that the intensity is constant at some arbitrary value during a time of stable polarity, drops to zero during a reversal for a time interval δ (here we use 40 kyr, but our results are not sensitive to the exact detail) and then recovers immediately following the reversal. During stable polarity times the dipole moment $p(t)$ is set to an appropriate average value. The time-series is sampled at $\Delta T = 1$ kyr for purposes of calculating the power spectrum as described later.

2.2 New composite spectrum

A separate multitaper power spectral density (PSD) estimate was derived for each of the time-series in Fig. 1 and the GTS12 record of Fig. S1. In each case we used a fixed number (10) of sine multitapers and pre-whitened with a 3rd order autoregressive process (Riedel & Sidorenko 1995, 1996). The results are shown in Fig. 2 and are colour coded according to the various time-series. Dense time sampling (ΔT as given in Table 1) avoids aliasing, but reveals the limitations in resolution for each time-series. The spectral estimate for each time-series lies below the next higher resolution one above some critical frequency. Using the preliminary composite spectrum in Fig. 2 we estimated the temporal resolution given in column 5 of Table 1 for each model's time-series and trimmed each spectral estimate above the truncation frequencies given in column 7 (these are just the reciprocal of the temporal resolutions). The truncated spectrum, shown in Fig. 3, provides a more reliable estimate for a composite spectrum. Overlapping estimates now lie within the uncertainties provided with the exception of the lowest frequency estimates derived from *gufm1*. It is possible that these

Table 1. Properties of time-series of axial dipole moments.

Description	Time span	Knot spacing (yr)	Sampling ΔT (yr)	Model res (yr)	Δf (Myr^{-1})	Trunc f (Myr^{-1})
GTS12	0–157.8 Ma	n/a	1000	50 000	0.06	20
PADM2M	0–2 Ma	1000	1000	5000	4.2	200
GGF100k	0–100 ka	200	100	1000	85.6	1000
CALS10k.2	0–10 ka	40	20	500	854	2000
HFM.OL1.A1	0–10 ka	40	20	200	854	5000
arhimag1k	1000–2000 CE	10	5	15	7645	60 000
gufm1_short	1840–1990 CE	2.5	1	4	5.5×10^4	250 000

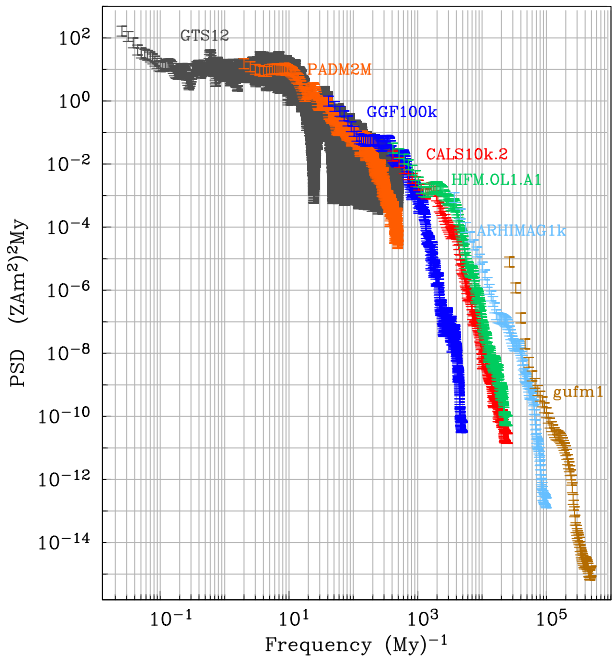

Figure 2. Composite power spectrum based on the times series shown in Figs 1 and S1. Error bars are one standard deviation. See text for discussion of reliability.

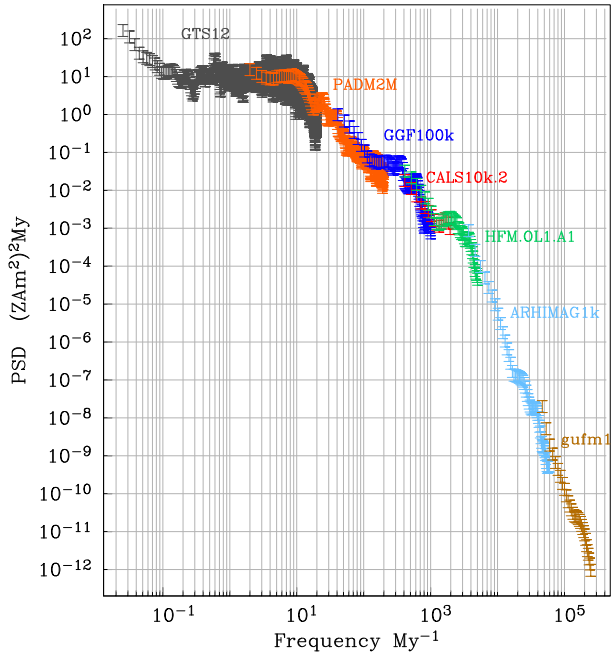

Figure 3. Trimmed composite power spectrum based on the times-series shown in Figs 1 and S1. Error bars are one standard deviation. See text for discussion of trimming from Fig. 2. Fig. S2 shows the frequency resolution in the composite spectrum.

may be strongly influenced by spectral leakage due to the recent decay in dipole strength, and they have also been trimmed in Fig. 3. Column 6 in Table 1 is the frequency resolution of the PSD pertinent to each time-series which is controlled by number of sinusoidal tapers (κ), $\Delta f = \frac{\kappa}{N}$, where N is the total number of points in the time-series. See Fig. S2 for a plot of the frequency resolution across the composite spectrum.

As was previously noted by Constable & Johnson (2005) we can loosely partition the spectrum into several frequency bands: For GTS12, 0.02–.2 Myr^{-1} represents changes in reversal frequency; the more or less flat part for 0.2–10 Myr^{-1} can be considered to represent average reversal rate; the falloff in GTS 12 above 10 Myr^{-1} is controlled by the product of reversal rate and specified duration of reversals in the artificially structured series, but agrees well with PADM2M; between 10 and 40 Myr^{-1} we see a general fall-off in the PADM2M spectrum with a bump in the range 20–30 Myr^{-1} that has been discussed as a possible representation of cryptochron and excursion rates (see Constable *et al.* 1998; Smith-Boughner *et al.* 2011), but this is not a well-resolved peak; in both PADM2M and GGF100k we see smooth decay above 40 Myr^{-1} and a flattening at around 100–300 Myr^{-1}; more hints of structure recur in the 400–4000 Myr^{-1} range in the form of departures from a monotonically decaying trend, and again above 10 000 and 100 000 Myr^{-1}. Underlying these incompletely resolved bumps in our spectral estimates is an overall red spectrum which we can characterize by successively higher power law falloff with increasing frequency. This underlying trend motivates stochastic modelling of dipole moment variations in the next section, where we seek to resolve four regimes for changes in dipole moment, based on (1) average reversal and excursion frequencies <20 Myr^{-1}; (2) time taken for reversals and other significant dipole moment variations on millennial timescales $\geq 20-5000$ My^{-1}; (3) centennial scale variations $\geq 5000-50\,000$ Myr^{-1} and (4) short-term variations $\geq 50\,000$ Myr^{-1}. We return to the question of structure in the composite spectrum in addition to the trend in Section 5.4. In this work we do not attempt to account for the very low frequency changes in reversal rate.

3 A NEW STOCHASTIC MODEL

Previous stochastic models have not used data extending across the entire frequency range of the composite spectrum, and at the highest frequencies, the new composite spectrum transitions to steeper spectral slopes than previous models allow. So we build a new, AR3 model for ADM variability that spans the entire frequency range of the composite spectrum and accommodates this steeper, spectral regime at highest frequencies.

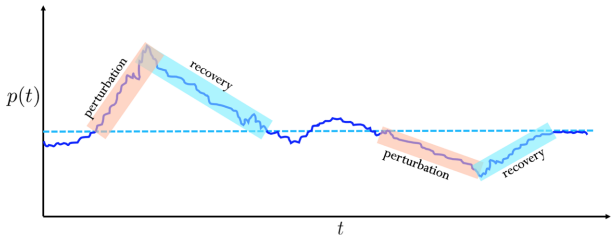

Figure 4. Axial dipole moment (solid, dark blue) perturbations (brown shadow) away from and recovery (blue shadow) back to time-averaged equilibrium (blue dashed line).

3.1 Continuous AR models

The temporal evolution of the ADM is not a memoryless process, and the ADM at time t is influenced by:

(i) The rate at which it has changed in the past until time t, $\frac{\mathrm{d}p}{\mathrm{d}t}$.
(ii) The way in which that rate itself has changed until time t, $\frac{d^2p}{\mathrm{d}t^2}$.
(iii) Higher-order derivatives, that is $\frac{d^3p}{\mathrm{d}t^3}$, $\frac{d^4p}{\mathrm{d}t^4}$ and so on.

Meanwhile, interactions across other parts of the geodynamo sometimes perturb the ADM away from its tendency to behave according to its own past. For example, fluid turbulence in the outer core influences the geomagnetic field in a way that is not deterministic with respect to time. Fluid turbulence thereby introduces stochastic behaviour into the evolution of $p(t)$. We represent the turbulent source of the perturbations as uncorrelated, white noise, $\zeta(t)$.

The ADM at time t can be written as:

$$p(t) = \alpha_1 \frac{\mathrm{d}p}{\mathrm{d}t} + \alpha_2 \frac{d^2p}{\mathrm{d}t^2} + \alpha_3 \frac{d^3p}{\mathrm{d}t^3} + \ldots + \zeta(t). \tag{3}$$

Each α_i is an amplitude that scales the relative impact of the corresponding derivative term on $p(t)$. $\zeta(t)$ can also be thought of as a forcing function that introduces new information into the system at uncorrelated times. We call eq. (3) a 'continuous autoregressive (AR)' equation. We use as many derivatives to describe the ADM as is prudent; when the equation extends out to the nth derivative, then we call it an 'ARn' equation.

3.2 A Langevin model

The AR equation is not the only way to describe the ADM's behaviour with time. Buffett et al. (2013) proposed using a Langevin description, which posits that variations of the ADM with respect to time are, in their terminology, dictated by 'diffusion' or *perturbation* away from an equilibrium state and 'drift', or *recovery* to equilibrium. Instead of calling these diffusion and drift (which seem appropriate for water molecules) we will use the terms *perturbation* and *recovery* to avoid confusion with the physical effects of Ohmic diffusion that play an important role in magnetic field decay in geomagnetism.

To describe this phenomenon Buffett *et al.* (2013) used the Langevin equation:

$$\frac{\mathrm{d}p}{\mathrm{d}t} = v(p) + \sqrt{D(p)}\Gamma(t). \tag{4}$$

Here $v(p)$ is our *recovery* term and $\sqrt{D(p)}\Gamma(t)$ represents the *perturbation*. Fig. 4 illustrates what recovery and perturbation mean in this context. The recovery term describes how the ADM returns to equilibrium after being perturbed away, and is assumed to represent both Ohmic diffusion and deterministic advection influencing the geodynamo. The dashed line in Fig. 4 is the value of the ADM when the axially dipolar geomagnetic field is in its most stable energy configuration. We assume that this equilibrium value is also the time-averaged ADM, $\bar{p}$, implying a stationary stochastic process.

As discussed before, fluid turbulence in Earth's outer core continuously introduces stochastic behaviour into the evolution of the ADM, $p(t)$. At any time t, stochastic influences might perturb the ADM away from equilibrium. This perturbation away from equilibrium is highlighted in light brown in Fig. 4. The probability that a perturbation will occur and the strength of the perturbation at time t are both described statistically.

After a perturbation occurs, the ADM recovers towards its equilibrium state, as highlighted in light blue in Fig. 4. We suppose that this recovery is deterministic and is linked to the magnetic induction equation that drives the geodynamo. Hence the ADM is constantly being perturbed away from equilibrium and then trying to recover.

The perturbation term has two parts: $\Gamma(t)$ describes the statistical distribution of the perturbation at time t, including any temporal correlations and $\sqrt{D(p)}$ is a stochastic function that scales the amplitude of the perturbation. In a time-series of $p(t)$, we can measure the influence of the perturbation term by measuring the standard deviation of the time-series. It turns out that $D(p)$ has units of variance, and the square root serves to translate the units into those of standard deviation.

3.3 Langevin → AR transformations

The AR eq. (3) is a linear differential equation whereas the Langevin eq. (4) is non-linear with respect to $p(t)$. Many mathematical methods have been developed to solve linear differential equations whereas far fewer have been developed to solve non-linear ones. Fortunately, prior work by Buffett *et al.* (2013), Bouligand *et al.* (2016) and Buffett & Matsui (2015) has demonstrated that we can assume specific functional forms for $v(p)$, $D(p)$ and $\Gamma(t)$ in the Langevin equation that transform the Langevin equation into an autoregressive one, as discussed below.

3.3.1 An AR1 model

First suppose that $\Gamma(t)$ is an uncorrelated (memoryless) process in time and random in amplitude so it can be equivalently represented as a white-noise, $\zeta(t)$, that is:

$$\Gamma(t) = \zeta(t). \tag{5}$$

To fit the Langevin model to known time-series like those of Fig. 1 for the ADM, we can make the following approximations:

$$v(p) \approx -\frac{p(t) - \bar{p}}{\tau_l} \tag{6}$$

$$D(\bar{p}) \approx D_{\mathrm{eq}} \tag{7}$$

where τ_l is the average time it takes for the ADM to recover to $\bar{p}$ after a perturbation away and D_{eq} is a constant value for the amplitude of the perturbation. Eq. (6) states that recovery occurs on timescale τ_l and that the recovery rate $v(p)$ for the ADM recovery is proportional to the amplitude of the perturbation, $p(t) - \bar{p}$. Eq. (7) states that the standard deviation of the ADM across time is roughly constant.

Applying these three approximations to the Langevin eq. (4) yields:

$$\frac{\mathrm{d}p'}{\mathrm{d}t} + \frac{p'(t)}{\tau_l} = \sqrt{D_{\mathrm{eq}}}\zeta(t) \tag{8}$$

where $p'(t) = p(t) - \bar{p}$. Eq. (8) describes an AR1 process.

3.3.2 An AR2 model

As discussed earlier, stochastic influences in Earth's outer core may be responsible for the perturbation introduced by $\Gamma(t)$. Buffett *et al.* (2013) assumed that $\Gamma(t)$ was uncorrelated in time and random in amplitude. Yet, the physical sources of stochastic information are unlikely to be well represented as totally uncorrelated noise in the geodynamo. Bouligand *et al.* (2016) subsequently made the approximation that $\Gamma(t)$ is an AR1 process and introduced a new timescale, τ_m, that describes how $\Gamma(t)$ maintains memory of its past:

$$\tau_m \frac{\mathrm{d}\Gamma}{\mathrm{d}t} + \Gamma(t) = \zeta(t), \tag{9}$$

with some memory from $\frac{\mathrm{d}\Gamma}{\mathrm{d}t}$ and some noisy influence from $\zeta(t)$. τ_m is the correlation timescale for the stochastic process, $\Gamma(t)$. Another way to look at it is by thinking of the physical sources of stochastic information in the geodynamo as having their own equilibrium behaviour, and random deviations away from equilibrium. In this line of thought, τ_m is the average time it takes the stochastic geodynamo process, like turbulence, to recover its equilibrium after a perturbation. When we apply the assumptions in eqs (9), (6) and (7), the Langevin equation becomes:

$$\tau_m \frac{d^2p'}{\mathrm{d}t^2} + \tau_m \left(\frac{1}{\tau_l} + \frac{1}{\tau_m}\right)\frac{\mathrm{d}p'}{\mathrm{d}t} + \frac{1}{\tau_l}p'(t) = \sqrt{D_{\mathrm{eq}}}\zeta(t). \tag{10}$$

Eq. (10) describes an AR2 process.

3.3.3 An AR2 spectrum

Taking the Fourier transform of eq. (10) and using some algebra produces a theoretical power spectrum for the AR2 process (Buffett & Matsui 2015):

$$S_{p'}(f) = \frac{2D_{\mathrm{eq}}}{\tau_m^2}\frac{1}{((4\pi^2 f^2 + \frac{1}{\tau_l^2})(4\pi^2 f^2 + \frac{1}{\tau_m^2})}. \tag{11}$$

The AR2 model spectrum, included as the longer, light-blue curve in Fig. 5, is flat at lowest frequencies, then goes like f^{-2} at mid-frequencies and finally like f^{-4} at high frequencies. Morzfeld & Buffett (2019) implemented a feature-based maximum likelihood approach to estimate their AR2 model parameters. The corresponding AR2 model spectrum (dashed black line) is plotted against the composite spectrum in Fig. 5. While it does a good job at low frequencies, it provides a poor match above 10^3 Myr^{-1}.

3.4 An AR3 model

In this paper, we additionally consider how to produce a theoretical spectrum that exhibits the f^{-6} regime that appears at highest frequencies in Fig. 3. To do this, we introduce a third timescale τ_s and assume that $\Gamma(t)$ is an AR2 process:

$$\tau_m\tau_s\frac{d^2\Gamma}{\mathrm{d}t^2} + \tau_m\tau_s\left(\frac{1}{\tau_m} + \frac{1}{\tau_s}\right)\frac{\mathrm{d}\Gamma}{\mathrm{d}t} + \Gamma(t) = \zeta(t). \tag{12}$$

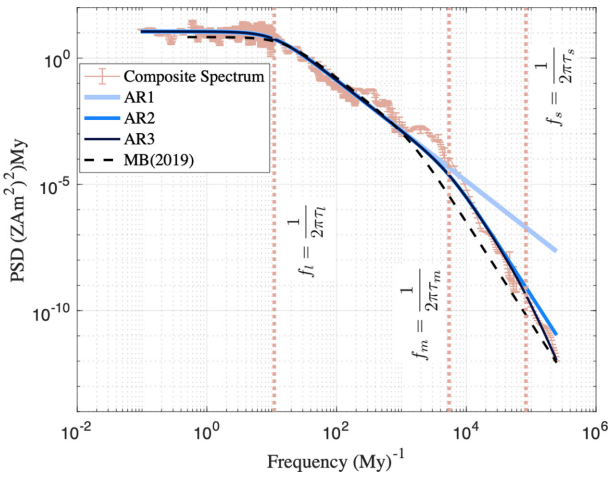

Figure 5. AR1, AR2 and AR3 model spectra that correspond to model parameters found by the LM algorithm (algorithm results are discussed in Section 4). The AR1 spectrum transitions from $S_{p'}(f) \propto \frac{1}{f^0}$ to $S_{p'}(f) \propto \frac{1}{f^2}$ at frequency f_l. The AR2 spectrum has a second transition to $S_{p'}(f) \propto \frac{1}{f^4}$ at frequency f_m. The AR3 spectrum has a third transition to $S_{p'}(f) \propto \frac{1}{f^6}$ at f_s. The dashed black curve is an AR2 model spectrum that corresponds to the model parameters for configuration *a* in table 6 of Morzfeld & Buffett (2019).

τ_s is thus another correlation timescale for $\Gamma(t)$. This suggests that the stochastic geodynamo processes that govern $\Gamma(t)$ actually have *two*, distinct, timescales that influence its recovery to equilibrium following a perturbation.

Next, we approximate the Langevin model using eqs (12), (6) and (7). This yields a new, AR3 equation for the temporal evolution of the ADM with time:

$$\frac{d^3p'}{\mathrm{d}t^3} + \left(\frac{1}{\tau_l} + \frac{1}{\tau_m} + \frac{1}{\tau_s}\right)\frac{d^2p'}{\mathrm{d}t^2} + \left(\frac{1}{\tau_l\tau_m} + \frac{1}{\tau_l\tau_s} + \frac{1}{\tau_m\tau_s}\right)\frac{\mathrm{d}p'}{\mathrm{d}t} + \left(\frac{1}{\tau_l\tau_m\tau_s}\right)p'(t) = \frac{\sqrt{D_{\mathrm{eq}}}}{\tau_m\tau_s}\zeta(t). \tag{13}$$

Finally, we take the Fourier transform (FT) of eq. (13), isolate $\tilde{P}(f)$ which is the FT of p' and square its absolute value to produce the AR3 model spectrum:

$$S_{p'}(f) = \frac{2D_{\mathrm{eq}}}{\tau_m^2\tau_s^2}\frac{1}{((4\pi^2 f^2 + \frac{1}{\tau_l^2})(4\pi^2 f^2 + \frac{1}{\tau_m^2})(4\pi^2 f^2 + \frac{1}{\tau_s^2})} \tag{14}$$

where

$$S_{p'}(f) = \mathcal{E}\left(|\tilde{P}(f)|^2\right) \tag{15}$$

$S_{p'}(f)$ is the frequency spectrum of the ADM and $\mathcal{E}$ is the expectation operator.

The AR3 model spectrum, included as the darkest curve in Fig. 5, is flat at lowest frequencies, falls off like f^{-2} at mid-frequencies, then goes like f^{-4} in the middle range of frequencies, and finally as f^{-6} at highest frequencies. The AR1, AR2 and AR3 model spectra are sketched for comparison in Fig. 5. The AR3 model spectrum steepens at highest frequencies in a way that the AR1 and AR2 models cannot. Note how the model parameters influence the shape of the power spectrum. In Fig. 5, we see that the transitions between f^{-n} regimes occur at corner frequencies labelled as $\{f_l, f_m, f_s\}$. From eq. (14) we obtain that our timescale parameters actually determine

the corner frequencies:

$$f_l = \frac{1}{2\pi\tau_l} \qquad f_m = \frac{1}{2\pi\tau_m} \qquad f_s = \frac{1}{2\pi\tau_s}. \tag{16}$$

So the timescale parameters determine how the shape of the AR3 model spectrum changes as we move from left to right. Meanwhile, by setting $f = 0$ in eq. (14) we see that:

$$S_{p'}(0) = D_{\rm eq}\, 2\tau_l^2. \tag{17}$$

So both $\{\tau_l, D_{\rm eq}\}$ determine how much power the AR3 model spectrum has at $f = 0$, and thereby the vertical scaling of the entire spectrum.

4 ESTIMATING MODEL PARAMETERS

We now seek an AR3 model that can accurately predict the statistical behaviour of the geomagnetic ADM as shown by the geomagnetic composite spectrum of Fig. 3. We look for best fitting values of $\{\tau_l, \tau_m, \tau_s, D_{\rm eq}\}$ in our model eq. (14) to the composite spectrum.

Since eq. (14) is a non-linear equation with respect to the τ's, we use the Levenberg–Marquardt (LM) algorithm (Levenberg 1944; Marquardt 1963) for non-linear least squares fitting. We calculate the uncertainties in our parameter estimates according to (Gavin 2020). To apply the LM algorithm to our problem we rewrite eq. (14) using the equivalences in eqs (16) and (17), replacing $\{D_{\rm eq}, \tau_l, \tau_m, \tau_s\}$ with $\{S_{p'}(0), f_l, f_m, f_s\}$. This yields:

$$S_{p'}(f) = \frac{S(0) f_l^2 f_m^2 f_s^2}{(f^2 + f_l^2)(f^2 + f_m^2)(f^2 + f_s^2)}. \tag{18}$$

We apply the LM algorithm to fit the composite spectrum in log domain, as in Fig. 3, to eq. (18). The results are given in Table 2 and plotted in Fig. 6.

Fig. 6 shows that the AR3 model (dark brown) generally provides a good fit to the composite spectrum with exceptions at some frequencies between 10^2 and 10^4 Myr^{-1} where there seems to be some excess power. We also show the AR2 LM solution obtained by fitting eq. (11) to the composite spectrum. Fig. 6 shows that the AR2 model (light blue) is a decent fit to the composite spectrum until $f = 10^5$ Myr^{-1}. Here, the AR2 model begins to deviate from the composite spectrum until it lies an entire order of magnitude above the composite spectrum at $f = 2.5 \times 10^5$ Myr^{-1}. The upper/lower bounds on the AR2 LM solution just barely enclose the composite spectrum, while the upper/lower bounds on the AR3 LM solution are more generous and easily enclose the composite spectrum. An AR3 model describes the composite spectrum better than AR2 at highest frequencies.

5 CONNECTIONS TO PHYSICAL PROCESSES IN THE GEODYNAMO

5.1 Diffusion versus advection

We turn now to the question of relating the τ's and $D_{\rm eq}$ uncovered in Table 2 to physical processes in Earth's core. The magnetic induction eq. (2) encapsulates two distinct aspects of changes in the magnetic field with time, namely diffusive decay and advection of the field by the fluid flow with velocity **v**. The latter might produce either growth or active decay in the dipole moment. At the large spatial scales represented by the axial dipole, the slowest changes in the geodynamo (long-term changes in thermal state and boundary conditions aside) are expected to be from Ohmic diffusion at the large length scales pertinent to Earth's outer core. The timescale for pure, Ohmic diffusion can be estimated by solving the magnetic diffusion equation that results from setting the flow velocity to zero:

$$\frac{\mathrm{d}\mathbf{B}}{\mathrm{dt}} = \frac{1}{\mu_0\sigma}\nabla^2\mathbf{B}. \tag{19}$$

An infinite number of solutions, $\mathbf{B}_n(r, \theta, \phi)$, exist for eq. (19) (e.g. Backus *et al.* 1996). All of them decay exponentially with respect to time, and the e-folding, decay timescale for the nth mode, τ_n, is given by

$$\tau_n = \frac{\mu_o \sigma r_c^2}{(n\pi)^2}, \tag{20}$$

where $r_c = 3\,480$ km is the approximate distance between the core–mantle boundary and Earth's center (Moffatt 1978), $\mu_o = 4\pi \times 10^{-7}$ H m^{-1} is the magnetic permeability in a vacuum and σ is the electrical conductivity of the outer core. The first decay mode, $n = 1$, corresponds to the slowest decay timescale.

If the electrical conductivity of the outer core is known, eq. (20) allows us to estimate the longest timescale associated with magnetic diffusion. Recent estimates of the electrical conductivity based on both *ab initio* calculations and mineral physics laboratory measurements now appear to lie in an interval ranging across $[0.5, 1.5] \times 10^6$ S m^{-1} (Pozzo *et al.* 2012; Berrada & Secco 2021). Choosing $\sigma = 0.9 \times 10^6$ S m^{-1} yields $\tau_1 = 43\,800$ yr, which is about three times as long as our estimate for the longest timescale in the AR3 model, $\tau_l = 14\,600 \pm 1\,700$ yr. Conversely, setting $\tau_l \approx \tau_1$ in eq. (20) to compute σ produces a value that does not fit within the range of published values, $[0.5, 1.5] \times 10^6$ S m^{-1}. If we suppose that we *should* have found $\tau_l = 43\,800$ yr, this would have implied a first corner frequency at $f_l \approx 3.634$ Myr^{-1}, a value that is clearly incompatible with our estimates of the power spectrum. We infer that $\tau_1 \neq \tau_l$.

5.1.1 *Higher Ohmic decay modes*

In fact we should not expect that $\tau_l = \tau_1$. The composite spectrum describes a geodynamo that incorporates advection in the perturbation and recovery process, while τ_1 is just the e-folding timescale for the first decay mode of pure, Ohmic diffusion with no advection.

The idea that $\tau_l < \tau_1$ has precedence. Using their AR2 model, Buffett & Puranam (2017) found $\tau_l = 13\,333$ yr while $\tau_1 \approx [24\,000, 73\,000]$ yr based on the conductivity range $\sigma \approx [0.5, 1.5] \times 10^6$ S m^{-1}. Previous studies using numerical geodynamo simulations at various Rayleigh numbers have also found that $\tau_l < \tau_1$ (Buffett 2014; Buffett & Matsui 2015). In the latter, the authors posited that τ_l must have roughly equal contributions from the decay modes τ_1 and τ_2.

We again take $\sigma = 0.9 \times 10^6$ S m^{-1} and use eq. (20) to obtain the Ohmic decay timescales (τ_1, τ_2 and τ_3) and associated corner frequencies for the first 3 decay modes in Table 3. The dotted blue curves in Fig. 7 show what happens to the AR3 model spectrum if we suppose that τ_l can be represented by each of the first 3 Ohmic decay modes. The long-dashed blue curve is an arbitrary linear combination of the dotted-blue spectra that closely matches the LM fit to the spectrum. It is essentially equivalent to the LM fit, exhibiting only slightly damped power near the first corner frequency. Thus, a linear combination of pure, Ohmic decay modes in action could provide an acceptable fit to the composite spectrum. However, this scenario is not physically plausible on its own because the influence of advection must also be considered in order to regenerate the dynamo.

Table 2. Estimates of our AR3 model parameters pertaining to features of the AR3 process in time and frequency domains.

Frequency domain	Time domain
$S_{p'}(0) = 11.23 \pm 1.04$ $(\mathrm{ZAm}^2)^2\mathrm{Myr}$	$D_{\mathrm{eq}} = 26440 \pm 3930$ $\frac{(\mathrm{ZAm}^2)^2}{\mathrm{Myr}}$
$f_l = 10.91 \pm 1.27$ Myr^{-1}	$\tau_l = 14580 \pm 1698$ yr
$f_m = 5.44 \pm 3.28 \times 10^3$ Myr^{-1}	$\tau_m = 29.3 \pm 17.6$ yr
$f_s = 8.30 \pm 11.86 \times 10^4$ Myr^{-1}	$\tau_s = 1.92 \pm 2.74$ yr

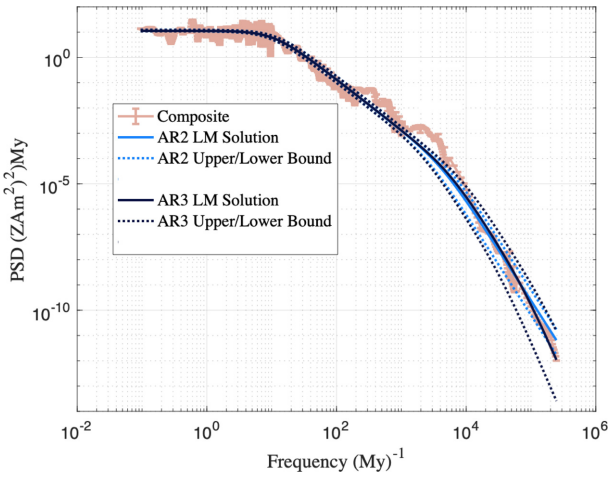

Figure 6. Levenberg–Marquardt (LM) solution produces an AR3 curve (dark brown) that mostly lies within the uncertainty region of the composite spectrum (light brown). Uncertainties in the LM estimates produce upper/lower bounds (dotted curves) on the LM solution. Fewer data lead to larger uncertainty in the LM-solution curve at high frequencies.

Table 3. Corner frequencies and e-folding timescales for several Ohmic decay modes.

n	τ_n (yr)	f_n (Myr^{-1})
1	43 800	3.6
2	10 950	14.5
3	4867	32.7

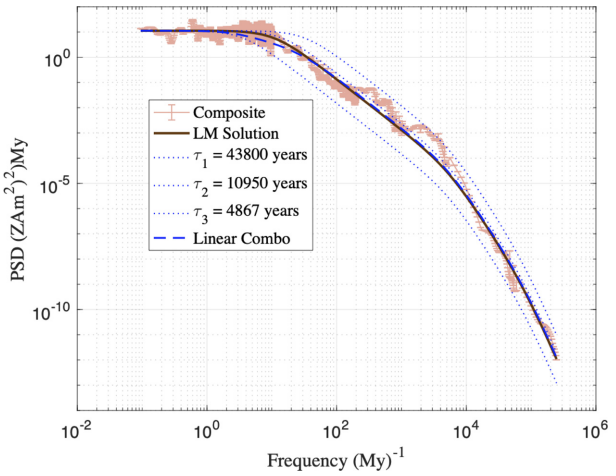

Figure 7. LM-solution (dark brown) and composite spectrum (light brown) against AR3 model spectra when $\tau_l \approx \tau_n$ is considered for decay modes $n = \{1, 2, 3\}$ (dotted-blue). An arbitrary linear combination of 3 decay-mode spectra (dashed-blue) closely matches the LM-solution (so closely that the dashed curve is visible only near transition frequency f_l). However, this cannot provide a complete physical representation for the spectrum.

5.1.2 *Adding turbulence to the mix*

An alternative and more physically plausible explanation for why $\tau_l < \tau_1$ makes sense involves *both* the higher Ohmic decay modes and fluid turbulence. Davis & Buffett (2021) suggested, based on results from numerical geodynamo simulations, that turbulence in Earth's outer core pumps energy into the dipole field and thus affects the shape of its power spectrum. Since turbulence occurs on smaller spatial scales, it likely produces magnetic field structures on spatial scales that are smaller than the dipole. However, it is expected that this energy seeps into the dipolar field; therefore, turbulence also guides energy into the dipolar frequency spectrum. We expect turbulence to influence the power at the highest frequencies of the spectrum.

We therefore consider what happens when turbulence is represented in the AR models by the noisy process, $\Gamma(t)$, which influences the spectrum at highest frequencies. One might infer that as turbulence pushes energy into the frequency spectrum, we would see a raised/shallower curve at highest frequencies. Yet the influence of turbulence on the dipole spectrum seems to depend on the autocorrelation we assume for $\Gamma(t)$. Switching from uncorrelated to doubly correlated $\Gamma(t)$ introduces f^{-4} and f^{-6} regimes and steepens the spectrum at highest frequencies. We propose two possible explanations for this. First, it is possible that representing turbulence as an uncorrelated, white-noise process pumps more energy into the dipole field while representing turbulence as a doubly correlated process pumps less energy into the dipole field and divests more energy into multipolar components of the field.

Alternatively, we may consider that $\Gamma(t)$ spreads its influence across the spectrum even into the lower frequencies, rather than being concentrated at highest frequencies. When $\Gamma(t)$ is doubly correlated, the resultant steepening at highest frequencies may not necessarily imply lessened energy beneath the spectrum: we posit that switching from uncorrelated to doubly correlated $\Gamma(t)$ actually moves the energy rooted in turbulence away from the highest frequencies and into the lower frequencies. This concept resembles an inverse energy cascade that allows the f^0 regime to stay high out to shorter timescales and pushes f_l further to the right than expected by τ_1 alone. Forward and inverse energy cascades have been shown to occur in planetary and astrophysical magnetic fields across spatial scales (Olson & Amit 2010; Huguet & Amit 2012), and in geophysical/astrophysical contexts across frequencies (Arbic *et al.* 2012, 2014). Energy cascades are of particular interest in magnetohydrodynamic turbulence and thus pose a useful mechanism to investigate geomagnetic field variability.

The concept that high-wavenumber flows like those of turbulence may drive an inverse energy cascade across frequencies has the potential to do better than the multimode purely diffusive scenario, which underestimated power near f_l between the dashed-blue and dark brown curves in Fig. 7. This hypothesis could be investigated by examining Earth-like numerical MHD simulations to analyse how high-wavenumber flows influence the frequency spectrum of the axial dipole field, but such an effort lies beyond the scope of this

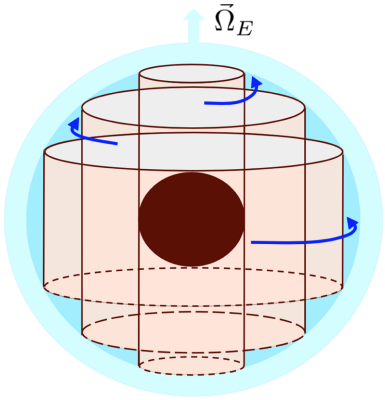

Figure 8. Three, discrete coaxial cylinders of fluid spinning either clockwise or counter-clockwise, as indicated by dark blue arrows. The cylinders are parallel to Earth's axis of rotation, Ω_E. The fluid columns oscillate back and forth relative to each other under competing influences of the Lorentz (magnetic) force and fluid inertia.

work. Nevertheless, a linear combination of the three Ohmic decay modes combined with advective influence elevating the power level near f_l, could produce the composite spectrum and the LM-fitted AR3 model. This suggests that Ohmic diffusion and advection in the geodynamo codrive the recovery of the ADM towards steady state.

5.2 Torsional oscillations in Earth's outer core

In our model the advective timescales in the geodynamo are represented by $\tau_m = 29 \pm 18$ yr and $\tau_s = 1.9 \pm 2.7$ yr. These are too short to correspond to overturn time of the outer core and we proposed earlier that they may be linked to helical eddies in the outer core. Helical turbulence has been shown to facilitate torsional oscillations under specific physical constraints (Moffatt & Dormy 2019). As a full evaluation of fluid turbulence is outside the scope of this paper, we do not go into the details here. Here, we simply note that the values of $\tau_m = 29 \pm 18$ yr and $\tau_s = 1.9 \pm 2.7$ yr may also point to torsional oscillations. We speculate later in Section 5.4 about the origin of some longer term features in the composite spectrum.

Braginsky (1970) showed that large-scale, columnar flows in Earth's outer core arise when we assume that Lorentz (magnetic), buoyancy and Coriolis forces equally influence fluid parcels in Earth's outer core. This flow structure is realistically a continuum of coaxial cylinders ranging from the core–mantle boundary to the inner-core boundary but as an approximation we can think of discrete, coaxial cylinders parallel to Earth's rotation axis as in Fig. 8.

To understand how torsional oscillations work, imagine an ambient magnetic field with a component that points cylindrically radially inward, $B_{\rm amb}$, passing through a fluid column rotating counter-clockwise. The fluid will try to align the field with the flow, pulling field vectors azimuthally (i.e. frozen flux approximation) away from its initial, radial state. To counter the changing radial/azimuthal magnetic fluxes, the Lorentz force induces a current back in the clockwise direction (i.e. Lenz's law), causing the fluid column to slow down. Then, fluid inertia propels the slowing column into the opposite, clockwise, flow direction. The fluid here pulls field vectors azimuthally again—this time clockwise—and then the Lorentz force attempts to bring the magnetic flux back to its initial state by inducing a counter-clockwise current; finally fluid inertia propels the column into counter-clockwise flow, and the whole thing starts over. Over time, the fluid columns oscillate back and forth relative to each other, producing 'torsional oscillations'.

Observational evidence suggests that torsional oscillations occur in Earth's outer core. Several studies have linked subdecadal variations in the geomagnetic field to torsional oscillations (Buffett *et al.* 2009; Cox *et al.* 2016). Gillet *et al.* (2010) inverted surface measurements of the geomagnetic field to generate core flow models that hinted at torsional oscillations operating in Earth's outer core. Torsional oscillations were also shown in numerical geodynamo simulations (Wicht & Christensen 2010; Teed *et al.* 2014, 2015). Several studies have related torsional oscillations to changes in the length of day (e.g. Holme & de Viron 2005), that are believed to occur on a 6-yr timescale.

There are actually many different modes of torsional oscillations, each with their own frequency and wavelength. The fundamental mode has period:

$$\tau_{\rm tor} = r_o \left(\frac{\rho_0 \mu_0}{B_{\rm amb}^2} \right)^{\frac{1}{2}} \approx 25 \text{ yr}, \tag{21}$$

where again $r_c = 3480$ km is the outer-core radius, $\rho_0 = 11\,000$ kg m^{-3} is the mean, outer-core density and $B_{\rm amb} = 0.5$ mT is the 'steady', background magnetic field (Finlay *et al.* 2010). However, the actual value of $B_{\rm amb}$ pertinent to Earth's outer core is not well known. If we assume that $B_{\rm amb} = 2$ mT, we would obtain $\tau_{\rm tor} \approx 6$ yr instead (Gillet *et al.* 2010).

We can plausibly link the fundamental mode of $\tau_{\rm tor} \approx 25$ yr to the value of $\tau_m = 29$ yr or the length of day signature $\tau_{\rm tor} \approx 6$ yr to $\tau_s = 1.9$ yr. Note that on the logarithmic scale of the composite spectrum, 1.9 and 6 yr will look nearly the same. Without a plausible estimate for $B_{\rm amb}$ or smaller uncertainties in our timescale estimates, we cannot tell if τ_m or τ_s pertain to torsional oscillations with certainty. However, the distinct timescales in our AR3 model might suggest the possibility of mode mixing across torsional oscillations as we discussed earlier for diffusive processes. For now, our stochastic model tentatively suggests that fluctuations of the ADM away from equilibrium could be partially due to torsional oscillations in Earth's outer core.

5.3 The rate of dipole recovery

The perturbation scale parameter, $D_{\rm eq} = 26440 \pm 3930$ (ZAm^2)^2 Myr^{-1}, represents $D(p)$ when $p(t)$ is near its steady-state value. In Section 3.2, we noted that $D(p)$ is proportional to the variance of the ADM. $D(p)$ actually has units of variance per unit time. The AR3 model variance is given by the integral of the power spectrum over all frequencies:

$$\sigma_{p'}^2 \equiv \int_{-\infty}^{\infty} S_{p'}(f) \mathrm{d}f, \tag{22}$$

which is evaluated from the spectrum of eq. (14) to obtain:

$$\sigma_{p'}^2 = \frac{D_{\rm eq}}{\tau_m^2 \tau_s^2} \left(\gamma_s \tau_l + \gamma_1 \tau_m + \gamma_2 \tau_s \right) \tag{23}$$

where the γ terms are non-linear combinations of $\{\tau_l, \tau_m, \tau_2\}$. We next solve for $D_{\rm eq}$ assuming that τ_m and τ_s are so small relative to τ_l that their influence is negligible:

$$D_{\rm eq} \approx \frac{\sigma_{p'}^2}{\tau_l}. \tag{24}$$

Taking $D_{\rm eq}$ and τ_l from Table 2, we get $\sigma_{p'} = 19.6$ ZAm^2, which is similar to the standard deviation of PADM2M (see Fig. 1 and

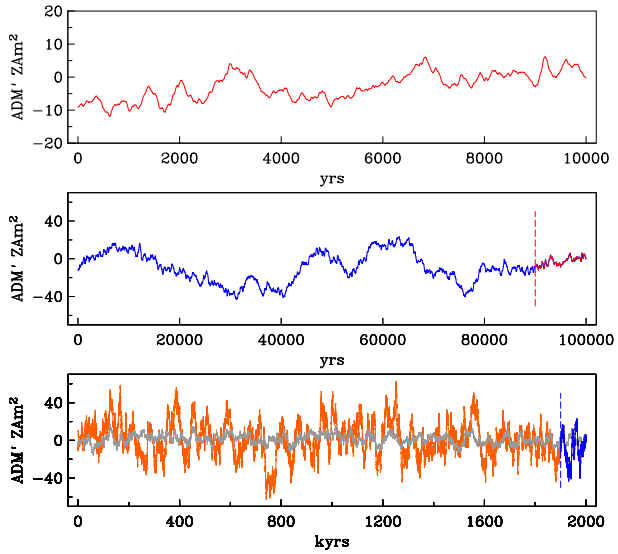

Figure 9. A single, 2 Myr (orange) numerical realization of $p^{'}$(t) (a zero-mean realization of ADM) for the AR3 process. Colors correspond to the same timescales as for Fig. 1, where PADM2M (Orange), GGF100k (blue) and CALS10k (red) are plotted. Gray line is the mean of 12 such realizations.

Ziegler *et al.* 2011,who give $\sigma_{\mathrm{PADM2M}} = 15.0\ \mathrm{ZAm}^2$). Another view is provided by simulating realizations of the AR3 process in the time domain using an Euler discretization procedure in Matlab. Fig. 9 shows a single realization of variations in $p^{'}(t)$ over 2 Myr, plotted in the same way as the palaeomagnetic data series of Fig. 1, although the mean value seen in the real ADMs is not reflected in the $p^{'}(t)$ simulations shown here. The gray curve in the lowermost panel presents an average across 12 separate realizations, with each realization spanning 2 Myr and having a time step of 1 yr. The average standard deviation value across all 12 realizations is 19.8 ZAm^2, which is close to the standard deviation predicted by eq. (24). The broad statistical similarities between Figs 1 and 9 is what we would expect for a viable stochastic model, noting that the 1 yr sampling interval of our AR3 simulation naturally gives rise to generally higher frequency variations than can be recovered from the different and variable resolution palaeomagnetic time-series.

Eq. (24) looks like a rate of some kind. We know that the standard deviation, $\sigma_{p'}$, tells us approximately how much the ADM changes each time it is perturbed. We also know that the energy stored in the geomagnetic, axial dipole field is proportional to the squared ADM (Griffiths 2017). Hence, the variance, $\sigma^2_{p'}$, provides a measure of how much the energy in the axial dipole field changes at each perturbation.

Given that τ_l is the timescale for recovery (as in eq. 6), eq. (24) gives the rate at which the energy in the axial dipole field returns to steady state after being perturbed away. It seems that the axial dipole field is at its most stable configuration when $p(t) = \bar{p}$. Perturbations pump energy into the axial dipole field, rendering it unstable. The field recovers its stability at the rate indicated by D_{eq}.

5.4 Slow MC waves in Earth's outer core

Fig. 6 shows that the composite spectrum has two bumps that deviate from the AR3 model. These bumps occur at around 400 Myr^{-1} and 2000 Myr^{-1}, loosely corresponding to timescales of 2500 and 500 yr, respectively. Both of these lie within a theoretical range of periods for slow MC waves in Earth's outer core: 100–10 000 yr (Finlay *et al.* 2010). The lower value also corresponds to common approximations for the overturn time of Earth's outer core.

Slow MC waves arise when the Lorentz (magnetic) and Coriolis forces dominate the force balance acting on fluid parcels in Earth's outer core. Various instabilities can initiate a slow MC wave, including convective instabilities that introduce buoyant forces into the system. Observations suggest that slow MC waves are plausible in Earth's outer core. Jackson (2003) pointed out a sequence of alternating, positive and negative flux patches of radial magnetic field near Earth's equator. Finlay & Jackson (2003) showed that this wave train drifts westward with wave period of approximately 270 yr. This may be explained by a slow MC wave near the CMB that travels and pulls magnetic field along azimuthally. Bulk, zonal winds near the equator at the CMB could advect the entire wave westward so that its speed and frequency appear faster in our observations at Earth's surface (Finlay *et al.* 2010).

Empirical identification of MC waves has already been claimed. After filtering at periods below 2500 yr and removing the axisymmetric field signal, Nilsson *et al.* (2020) identified features in Holocene field models corresponding to westward drift at 1125 and 5000 yr in time longitude and radon drift plots. They link these periods to westward drift of high-latitude convection rolls (which form the major contribution to the axial dipole field) and/or magnetic Rossby waves.

Our AR3 model does not predict either of the two bumps in Fig. 6, and thus lacks any physical link to slow MC waves. Accommodating the two bumps at 2500 and 500 yr would require some differences to the f^{-2} power-law regime in that interval of our AR3 spectrum, and likely need to include explicit links to the non-axial dipole part of the field as is implicit in the filtering approach used by Nilsson *et al.* (2020). Nilsson *et al.* (2020) also provide observational evidence to support deviations from a purely AR model that are attributed to magnetic Rossby waves in the geodynamo. This is the subject of ongoing investigations.

6 CONCLUSIONS

We have presented time-series and a new composite spectrum that describe the secular variation of the geomagnetic ADM across timescales spanning 1 to 10^6 yr. Good agreement in frequency ranges where the composite parts overlap provide some confidence in the underlying structure. A stochastic, AR3 model describes the temporal variations in the ADM and successfully predicts large-scale trends of the new, composite spectrum. The power spectrum is used to estimate fundamental long, medium, and short timescales describing the secular variation that point to physical processes in the geodynamo. Based on these estimates, we inferred that torsional oscillations perturb the ADM away from a steady-state value, after which Ohmic diffusion and advection codrive energy transfer and the recovery of the ADM to its steady state. Deviations from our stochastic model in period ranges around 2500 and 500 yr likely also contribute to fundamental processes driving changes in the ADM and suggest additional sources of perturbations that are not well fit by the AR3 model for the axial dipole alone. We speculate that these deviations might be considered a fundamental characteristic of Earth-like dynamos, linked to magnetohydrodynamic waves.

ACKNOWLEDGMENTS

We thank Matthias Morzfeld, Christopher Davies and Sabine Stanley for very helpful discussions. This work was supported by the

United States National Science Foundation grants EAR 1623786 and 1953778. We thank two anonymous reviewers for helpful comments that led to improvements in the manuscript.

Author contribution: Mayuri Sadhasivan developed the new stochastic (AR3) model and analysed the connections to physical processes in the geodynamo. Catherine Constable conceived the project, built the new composite spectrum and contributed to refining the analysis of the connections to physical processes in the geodynamo. Mayuri Sadhasivan and Catherine Constable cowrote the paper.

DATA AVAILABILITY STATEMENT

The data and products contained in this paper will be made available in the Earth Reference Digital Archive ERDA at https://earthref.org/ERDA/2525 on publication of this paper. For any additional information, please contact the corresponding author.

REFERENCES

Alken, P. *et al.*, 2021. International geomagnetic reference field: the thirteenth generation, *Earth, Planets Space,* **73,** doi:10.1186/s40623-020-01288.

Arbic, B.K., Müller, M., Richman, J.G., Shriver, J.F., Morten, A.J., Scott, R.B., Sérazin, G. & Penduff, T., 2014. Geostrophic turbulence in the frequency-wavenumber domain: Eddy-driven low-frequency variability, *J. Phys. Oceanogr.,* **44,** 2050–2069.

Arbic, B.K., Scott, R.B., Flierl, G.R., Morten, A.J., Richman, J.G. & Shriver, J.F., 2012. Nonlinear cascades of surface oceanic geostrophic kinetic energy in the frequency domain, *J. Phys. Oceanogr.,* **42,** 1577–1600.

Avery, M.S., Constable, C.G., Davies, C.J. & Gubbins, D., 2019. Spectral methods for analyzing energy balances in geodynamo simulations., *Phys. Earth planet. Inter.,* **286,** 127–137.

Backus, G., Parker, R. & Constable, C., 1996. *Foundations of Geomagnetism,* Cambridge Univ. Press.

Bengtsson, L., 2003. Periodic and non-periodic processes in the Earth's atmosphere and oceans, and their relevance for climate prediction, in *Interplay of Periodic, Cyclic and Stochastic Variability in Selected Areas of the H-R Diagram,* Vol. **292,** pp. 433, Astronomical Society of the Pacific Conference Series.

Berhanu, M. *et al.*, 2007. Magnetic field reversals in an experimental turbulent dynamo, *Europhys. Lett. (EPL),* **77**(5), 59001, doi:10.1209/0295-5075/77/59001.

Berrada, M. & Secco, R.A., 2021. Review of electrical resistivity measurements and calculations of Fe and Fe-alloys relating to planetary cores, *Front. Earth Sci.,* **9,** doi:10.3389/feart.2021.732289.

Bouligand, C., Gillet, N., Jault, D., Schaeffer, N., Fournier, A. & Aubert, J., 2016. Frequency spectrum of the geomagnetic field harmonic coefficients from dynamo simulations, *Geophys. J. Int.,* **207,** 1142–1157.

Braginsky, S. I., 1970. Torsional Magnetohydrodynamic Vibrations in the Earth's Core and Variations in Day Length, *Geomagnetism and Aeronomy,* **10,** 1.

Buffett, B., 2014. Geomagnetic fluctuations reveal stable stratification at the top of the earth?s core, *Nature,* **507,** 484–487.

Buffett, B. & Matsui, H., 2015. A power spectrum for the geomagnetic dipole moment, *Earth planet. Sci. Lett.,* **411,** 20–26.

Buffett, B. & Puranam, A., 2017. Constructing stochastic models for dipole fluctuations from paleomagnetic observations, *Phys. Earth planet. Inter.,* **272,** 68–77.

Buffett, B.A., King, E.M. & Matsui, H., 2014. A physical interpretation of stochastic models for fluctuations in the earth's dipole field, *Geophys. J. Int.,* **198,** 597–608.

Buffett, B.A., Mound, J. & Jackson, A., 2009. Inversion of torsional oscillations for the structure and dynamics of earth's core, *Geophys. J. Int.,* **177,** 878–890.

Buffett, B.A., Ziegler, L. & Constable, C.G., 2013. A stochastic model for palaeomagnetic field variations, *Geophys. J. Int.,* **195**(1), 86–97.

Cande, S.C. & Kent, D.V., 1995. Revised calibration of the geomagnetic polarity timescale for the late cretaceous and cenozoic, *J. geophys. Res.,* **100,** 6093–6095.

Constable, C., 2000. On rates of occurrence of geomagnetic reversals, *Phys. Earth planet. Inter.,* **118,** 181–193.

Constable, C. & Johnson, C., 2005. A paleomagnetic power spectrum, *Phys. Earth planet. Inter.,* **153,** 61–73.

Constable, C., Korte, M. & Panovska, S., 2016. Persistent high paleosecular variation activity in southern hemisphere for at least 10000 years, *Earth planet. Sci. Lett.,* **453,** 78–86.

Constable, C.G., Tauxe, L. & Parker, R.L., 1998. Analysis of 11 myr of geomagnetic intensity variation, *J. geophys. Res.,* **103,** 17 735–17 748.

Cox, A., 1968. Lengths of geomagnetic polarity reversals, *J. geophys. Res.,* **73,** 3247–3260.

Cox, A., Doell, R.R. & Dalrymple, G.B., 1964. Reversals of the earth's magnetic field, *Science,* **144,** 1537–1543.

Cox, G., Livermore, P. & Mound, J., 2016. The observational signature of modelled torsional waves and comparison to geomagnetic jerks, *Phys. Earth planet. Inter.,* **255,** 50–65.

Davies, C.J. & Constable, C.G., 2014. Insights from geodynamo simulations into long-term geomagnetic field behavior, *Earth planet. Sci. Lett.,* **404,** 238–249.

Davis, W. & Buffett, B., 2021. Inferring core processes using stochastic models of the geodynamo, *Geophys. J. Int.,* **228**(3), 1478–1493.

Di Lorenzo, E., Cobb, K.M., Furtado, J.C., Schneider, N., Anderson, B.T., Bracco, A., Alexander, M.A. & Vimont, D.J., 2010. Central pacific el niño and decadal climate change in the north pacific ocean, *Nat. Geosci.,* **3,** 762–765.

Finlay, C., Dumberry, M., Chulliat, A. & Pais, M., 2010. Short timescale core dynamics: theory and observations, *Space Sci. Rev.,* **155,** 177–218.

Finlay, C. & Jackson, A., 2003. Equatorially dominated magnetic field change at the surface of earth's core, *Science,* **300,** 2084–2086.

Finlay, C.C., Olsen, N., Kotsiaros, S., Gillet, N. & Tøffner-Clausen, L., 2016. Recent geomagnetic secular variation from swarm and ground observatories as estimated in the CHAOS-6 geomagnetic field model, *Earth, Planets Space,* **68**(1), 112, doi:10.1186/s40623-016-0486-1.

Gavin, H.P., 2020. The Levenberg-Marquardt algorithm for nonlinear least squares curve-fitting problems.1–19

Gillet, N., Jault, D., Canet, E. & Fournier, A., 2010. Fast torsional waves and strong magnetic field within the earth?s core, *Nature,* **465,** 74–77.

Glass, B. & Heezen, B., 1967. Tektites and geomagnetic reversals, *Nature,* **214,** doi:10.1038/214372a0.

Griffiths, D.J., 2017. *Introduction to Electrodynamics,* 4th edn, Cambridge Univ. Press.

Gwirtz, K., Morzfeld, M., Fournier, A. & Hulot, G., 2021. Can one use earth's magnetic axial dipole field intensity to predict reversals?, *Geophys. J. Int.,* **225,** 277–297.

Hathaway, D.H., 2015. The solar cycle, *Living Rev. Solar Phys.,* **12,** 4–87.

Holme, R. & de Viron, O., 2005. Geomagnetic jerks and a high-resolution length-of-day profile for core studies, *Geophys. J. Int.,* **160**(2), 435–439.

Hoyng, P., Schmitt, D. & Ossendrijver, M., 2002. A theoretical analysis of the observed variability of the geomagnetic dipole field, *Phys. Earth planet. Inter.,* **130,** 143–157.

Huguet, L. & Amit, H., 2012. Magnetic energy transfer at the top of the earth's core, *Geophys. J. Int.,* **190,** 856–870.

Jackson, A., 2003. Intense equatorial flux spots on the surface of the earth's core, *Nature,* **424,** 760–763.

Jackson, A., Jonkers, A. R.T. & Walker, M.R., 2000. Four centuries of geomagnetic secular variation from historical records, *Phil. Trans. R. Soc., A,* **358,** 957–990.

Korte, M. & Constable, C., 2003. Continuous global geomagnetic field models for the past 3000 years, *Phys. Earth planet. Inter.,* **140,** 73–89.

Langevin, P., 1908. Sur la théorie due mouvement brownien, *C. R. Acad. Sci. (Paris),* **146,** 530–533.

Levenberg, K., 1944. A method for the solution of certain non-linear problems in least squares, *Q. Appl. Math.,* **2,** 164–168.

Marquardt, D., 1963. An algorithm for least-squares estimation of nonlinear parameters, *J. Soc. Indust. Appl. Math.,* **11,** 431–441.

McFadden, P.L., Merrill, R.T. & McElhinny, M.W., 1988. Dipole/quadrupole family modeling of paleosecular variation, *J. geophys. Res.,* **93**(B10), 11583–11588.

Moffatt, H.K., 1978. *Magnetic Field Generation in Electrically Conducting Fluids,* Cambridge Univ. Press.

Moffatt, K. & Dormy, E., 2019. *Helical Turbulence,* pp. 417–440, Cambridge Univ. Press.

Morzfeld, M. & Buffett, B.A., 2019. A comprehensive model for the kyr and myr timescales of Earth's axial magnetic dipole field, *Nonlin. Process. Geophys.,* **26,** 123–142.

Nilsson, A., Muscheler, R. & Snowball, I., 2011. Millennial scale cyclicity in the geodynamo inferred from a dipole tilt reconstruction, *Earth planet. Sci. Lett.,* **311,** 299–305.

Nilsson, A., Suttie, N., Korte, M., Holme, R. & Hill, M., 2020. Persistent westward drift of the geomagnetic field at the core-mantle boundary linked to recurrent high-latitude weak/reverse flux patches, *Geophys. J. Int.,* **222,** 1423–1432.

Ogg, J., 2012. Chapter 5 - geomagnetic polarity time scale, in *The Geologic Time Scale,* pp. 85–113, eds Gradstein, F.M., Ogg, J.G., Schmitz, M.D. & Ogg, G.M., Elsevier.

Olsen, N., Lühr, H., Finlay, C.C., Sabaka, T.J., Michaelis, I., Rauberg, J. & Tøffner-Clausen, L., 2014. The chaos-4 geomagnetic field model, *Geophys. J. Int.,* **197,** 815–827.

Olson, P. & Amit, H., 2010. A dynamo cascade interpretation of the geomagnetic dipole decrease, *Geophys. J. Int.,* **181,** 1411–1427.

Olson, P.L., Christensen, U.R. & Driscoll, P.E., 2012. From superchrons to secular variation: a broadband dynamo frequency spectrum for the geomagnetic dipole, *Earth planet. Sci. Lett.,* **319–320,** 75–82.

Panovska, S., Constable, C.G. & Korte, M., 2018. Extending global continuous geomagnetic field reconstructions on timescales beyond human civilization, *Geochem. Geophys. Geosyst.,* **19**(12), 4757–4772.

Pétrélis, F. & Fauve, S., 2008. Chaotic dynamics of the magnetic field generated by dynamo action in a turbulent flow, *J. Phys.: Conden. Matter,* **20**(49), 494203, doi:10.1088/0953-8984/20/49/494203.

Pétrélis, F. & Fauve, S., 2010. Mechanisms for magnetic field reversals, *Phil. Trans. A, Math., Phys., Eng. Sci.,* **368,** 1595–605.

Pozzo, M., Davies, C., Gubbins, D. & Alfè, D., 2012. Thermal and electrical conductivity of iron at earth's core conditions, *Nature,* **485,** 355–358.

Riedel, K.S. & Sidorenko, A., 1995. Minimum bias multiple taper spectral estimation, *IEEE Trans. Signal Proc.,* **43,** 188–195.

Riedel, K.S. & Sidorenko, A., 1996. Adaptive smoothing of the log spectrum with multiple tapering, *IEEE Trans. Signal Proc.,* **44,** 1794–1800.

Schmitt, D., Ossendrijver, M. & Hoyng, P., 2001. Magnetic field reversals and secular variation in a bistable geodynamo model, *Phys. Earth planet. Inter.,* **125,** 119–124.

Senftleben, R., 2020. Earth's magnetic field over the last 1000 years, *PhD thesis*, University of Potsdam, Germany.

Smith-Boughner, L., Ziegler, L. & Constable, C., 2011. Changing spectrum of geomagnetic intensity variations in a fragmented 12 My sediment record from the oligocene, *Phys. Earth planet. Inter.,* **188**(3), 260–269.

Teed, R.J., Jones, C.A. & Tobias, S.M., 2014. The dynamics and excitation of torsional waves in geodynamo simulations, *Geophys. J. Int.,* **196,** 724–735.

Teed, R.J., Jones, C.A. & Tobias, S.M., 2015. The transition to Earth-like torsional oscillations in magnetoconvection simulations, *Earth planet. Sci. Lett.,* **419,** 22–31.

Valet, J.-P., Meynadier, L. & Guyodo, Y., 2005. Geomagnetic dipole strength and reversal rate over the past two million years, *Nature,* **435,** 802–805.

Wicht, J. & Christensen, U.R., 2010. Torsional oscillations in dynamo simulations, *Geophys. J. Int.,* **181,** 1367–1380.

Yamazaki, T. & Oda, H., 2002. Orbital influence on Earth's magnetic field: 100,000-year periodicity in inclination, *Science,* **295,** 2435–2438.

Ziegler, L.B., Constable, C.G., Johnson, C.L. & Tauxe, L., 2011. PADM2M: a penalized maximum likelihood model of the 0-2 Ma palaeomagnetic axial dipole moment, *Geophys. J. Int.,* **184,** 1069–1089.

SUPPORTING INFORMATION

Supplementary data are available at *GJI* online.

Figure S1. Polarity information time-series for 0–160 Ma from GTS12. Each polarity interval is represented by constant dipole intensity that drops to zero for $\delta \approx 30$ kyr during a reversal.

Figure S2. Frequency resolution in the composite spectrum.

Please note: Oxford University Press is not responsible for the content or functionality of any supporting materials supplied by the authors. Any queries (other than missing material) should be directed to the corresponding author for the paper.